sion rate at low temperature, a key parameter, has been extrapolated from ~1000°C (*14*). A decrease in either the diffusion rate or the exsolution time would increase the minimum temperature of the solvus.

Thus, the exsolution lamellae in Divnoe olivines are consistent with a miscibility gap in Fe-Mg olivine at temperatures higher than ~150°C. Among known models of olivine solid solutions only that of Sack and Ghiorso is consistent with this limit. In this model (*6*), equilibrium requires that homogeneous Divnoe olivines should exsolve into two phases with different compositions—Fa_{20-25} and Fa_{75-80}—below ~300°C, or at a lower temperature if strain and surface energies are taken into account. At temperatures <200°C, a spontaneous spinodal decomposition can occur. At the higher exsolution temperatures predicted by the model of (*6*), the time required for exsolution would be reduced to more realistic values. The major discrepancy between our data and the model of (*6*) is the compositional difference between lamellae. If the lamellae in Divnoe olivines are equilibrated, as their compositions indicate, then the small compositional differences between lamellae and their positions on the Mg-rich side of the diagram may define the crest of an asymmetric solvus dome rather than the idealized symmetric solvus proposed by (*6*). An asymmetric olivine solvus has been suggested (*4, 5, 7, 16*), but all models predict its maximum at Fe-rich rather than Mg-rich compositions. Our data strongly suggest a solvus crest at around Fa_{26}, which is in agreement with experimental data by Schulien (*17*), who found compositionally different olivines (Fa_{28} and Fa_{49} at 420°C, Fa_{17} and Fa_{57} at 400°C) coexisting with aqueous solutions of $(Fe,Mg)Cl_2$. If Schulien's data are correct, then the temperature of the solvus crest could be as high as ~450°C, and exsolved olivine grains may be found in some meteorites and terrestrial basic plutons that experienced very slow cooling.

REFERENCES AND NOTES

1. W. A. Deer *et al.*, *Rock-forming Minerals*. vol. 1A, *Orthosilicates* (Longman, London, 1982).
2. G. E. Brown Jr., in *Orthosilicates*, P. H. Ribbe, Ed., vol. 5 of *Reviews in Mineralogy* (Mineralogical Society of America, Washington, DC, ed. 2, 1982), pp. 275–392.
3. R. H. Nafziger and A. Muan, *Am. Mineral.* **52**, 1364 (1967).
4. K. Kitayama and T. Katsura, *Bull. Chem. Soc. Jpn.* **41**, 1146 (1968).
5. B. J. Wood and O. J. Kleppa, *Geochim. Cosmochim. Acta* **45**, 529 (1981).
6. R. O. Sack and M. S. Ghiorso, *Contrib. Mineral. Petrol.* **102**, 41 (1989).
7. N. M. Wiser and B. J. Wood, *ibid.* **108**, 146 (1991).
8. M. I. Petaev *et al.*, *Meteoritics* **29**, 182 (1994).
9. M. I. Petaev, *Lunar Planet. Sci.* **24**, 1127 (1993).
10. Back-scattered electron images were obtained on a JEOL 733 Superprobe operating at 15 kV with a 20-nA beam current. Routine electron microprobe analyses were performed at the same conditions with a spatial resolution of ~3 μm defined as the diameter of the electron interaction hemispheric volume (*18*). Fine-scale probing was done on the same instrument at an accelerating voltage of 10 kV, with spatial resolution of ~1.5 μm. Transmission electron microscopy was performed on ion-milled samples of olivine that had been previously characterized by electron microprobe and BSE analysis. A JEOL 2000FX analytical transmission electron microscope operating at 200 kV was used throughout. In situ quantitative analyses were obtained through use of a Tracor Northern TN 5500 EDS system with a Be-window detector.
11. M. I. Petaev and A. J. Brearley, *Lunar Planet. Sci.* **25**, 1069 (1994).
12. I. Parsons and W. L. Brown, in *Diffusion, Atomic Ordering and Mass Transport*, J. Ganguly, Ed. (Springer-Verlag, New York, 1991), pp. 304–344; A. Putnis, *Introduction to Mineral Sciences* (Cambridge Univ. Press, New York, 1992).
13. The wavelength (λ) of a spinodal structure, the time (τ) needed to produce it, and the diffusion rate (D_t) are related by the equation $\lambda^2 = \tau D_t$ (*19*). Variations of the diffusion rate with temperature are described by the equation $D_t = 9.6 \times 10^{-9} \exp(-15888/T)$, which is derived from experimental data (*14*) corrected for compositional and redox differences.
14. D. K. Buening and P. R. Buseck, *J. Geophys. Res.* **78**, 6852 (1973).
15. M. Morioka and H. Nagasawa, in *Diffusion, Atomic Ordering and Mass Transport*, J. Ganguly, Ed. (Springer-Verlag, New York, 1991), pp. 176–197.
16. R. J. Williams, *Earth Planet. Sci. Lett.* **15**, 296 (1972).
17. S. Schulien, *Contrib. Mineral. Petrol.* **74**, 85 (1980). Estimates of olivine compositions were based on x-ray diffraction patterns with an accuracy of 5% in the most favorable conditions.
18. J. I. Goldstein *et al.*, *Scanning Electron Microscopy and X-ray Microanalysis* (Plenum, New York, 1981).
19. J. W. Cahn, *Trans. Metall. Soc. AIME* **242**, 166 (1968).

20. We thank NASA for financial support (grants NAGW-3451 to J.A.W. and NAGW-3347 to J.J.P.). Transmission electron microscopy was carried out in the Electron Microbeam Analysis Facility, Department of Earth and Planetary Sciences and Institute of Meteoritics, University of New Mexico.

2 June 1994; accepted 28 September 1994

Teleseismic Search for Slow Precursors to Large Earthquakes

Pierre F. Ihmlé and Thomas H. Jordan*

Some large earthquakes display low-frequency seismic anomalies that are best explained by episodes of slow, smooth deformation immediately before their high-frequency origin times. Analysis of the low-frequency spectra of 107 shallow-focus earthquakes revealed 20 events that had slow precursors (95 percent confidence level); 19 were slow earthquakes associated with the ocean ridge–transform system, and 1 was a slow earthquake on an intracontinental transform fault in the East African Rift system. These anomalous earthquakes appear to be compound events, each comprising one or more ordinary (fast) ruptures in the shallow seismogenic zone initiated by a precursory slow event in the adjacent or subjacent lithosphere.

Low-frequency teleseismic signals contain information about earthquake rupture processes that is crucial to understanding large earthquakes of long duration. Standard waveform-modeling procedures poorly constrain the source spectrum below about 7 to 10 mHz, but newer techniques, based on the averaging of amplitude and phase-delay measurements over global networks of high-performance stations, yield good spectral resolution at seismic frequencies as low as 1 mHz (*1*). We recently synthesized the spectrum of the great Macquarie Ridge earthquake (23 May 1989) from 1 to 50 mHz from overlapping sets of free-oscillation, surface-wave, and body-wave measurements. We inferred from a series of spectral inversions that the main shock was initiated by a slow, smooth precursor that began several hundred seconds before the high-frequency origin time (*1*). Slow precursors large enough to be teleseismically detectable have been found for other large earthquakes in oceanic lithosphere, including the great Chilean earthquake of 22 May 1960 (*2*), the intermediate-focus Peru-Ecuador event of 12 April 1983 (*3*), and some slow earthquakes on the ocean ridge–transform system (*4*).

One can detect a slow precursor by comparing the origin time of an earthquake determined from high-frequency waves with an upper bound on its start time inferred from low-frequency waves (*3*). We used this approach to investigate three groups of shallow-focus earthquakes (Fig. 1). Group A is a set of 68 events associated with the ocean ridge–transform system, comprising essentially all of the well-recorded, large (moment magnitude $M_W \gtrsim 6.4$) earthquakes on or near mid-ocean ridge segments and oceanic transform faults between 1977 and 1992 (*5*). Group B is a sample of 23 earthquakes in zones of plate convergence, including 6 predominantly strike-slip events in volcanic arcs and back-arc basins. Group C comprises 1 normal, 11 strike-slip, and 4 reverse-faulting events

P. F. Ihmlé, Institut de Physique du Globe, 4 Place Jussieu, Paris Cedex 75252, France.
T. H. Jordan, Department of Earth, Atmospheric, and Planetary Sciences, Massachusetts Institute of Technology, Cambridge, MA 02139, USA.

*To whom correspondence should be addressed.

that occurred in continental crust (6). All of the earthquakes had Harvard centroid moment tensor (CMT) (7) depths of less than 50 km.

We estimated a total-moment (amplitude) spectrum $M_T(\omega)$ and time-shift (phase-delay) spectrum $\Delta t(\omega)$ of the source (8) at 1-mHz intervals from vertical-component, long-period recordings of 6 hours (9). We referenced the time-shift spectrum to the high-frequency origin time determined by the National Earthquake Information Center (NEIC). For most events, we fixed the spatial centroid and source mechanism at the Harvard CMT solutions (7), although we checked these parameters against our own determinations and sometimes modified the centroid depth. We recovered $\Delta t(\omega)$ up to 10 mHz by applying the phase-equalization method of Riedesel and Jordan (10) to fundamental-mode free oscillations. To estimate $M_T(\omega)$, we used the phase-incoherent spectral integration technique of Silver and Jordan (11), which does not require the isolation of individual spectral peaks and yields reliable spectral amplitudes up to 20 mHz. The synthetic seismograms used in the inversion accounted for propagation effects owing to anisotropic radial structure, ellipticity, and aspherical structure up to spherical harmonic degree 36 (12). In a number of cases when the data were available, we also estimated the source spectra using three other data sets: R_1 surface waves from vertical and radial components, toroidal-mode free oscillations from transverse components, and G_1 surface waves from transverse components. There was good agreement among the four methods, despite their differing sensitivities to earth structure (1, 13).

We fit the recovered spectra at frequencies from 1 to 10 mHz with the functions

$$M_T(\omega) = M_T^0(1+\omega^2\tau_c^2/8)^{-1} \qquad (1)$$

$$\Delta t(\omega) = (1-\alpha)\Delta t_1 + \frac{\alpha}{\omega}\arctan \omega\Delta t_1 \qquad (2)$$

(solid lines in the examples of Fig. 2) to obtain the four parameters M_T^0, τ_c, Δt_1, and α. The time-shift spectra tended to be flat and gave centroid time shifts Δt_1 that usually agreed with the higher frequency (>6 mHz) Harvard CMT solutions. For most of the group B and group C earthquakes, and some in group A, the total-moment spectra rolled off slowly (for example, the Flores Island, South of Australia, and Landers earthquakes of Fig. 2), implying that their characteristic durations τ_c were short, and our estimates of the total (zero-frequency) seismic moments M_T^0 generally agreed with the Harvard moments. For many earthquakes in group A (Prince Edward Island, Chile Transform, Macquarie Ridge, and Rivera Transform in Fig. 2) and a few in groups B (Nicaragua) and C (Sudan), however, the amplitudes decayed rapidly out to 10 mHz, indicating that they were sources of long duration; in these cases, the amplitude spectra were usually characterized by slope breaks at 6 to 12 mHz, and our estimates of M_T^0 were often larger than the Harvard CMT solutions.

For most of the events in groups B and C, the characteristic velocities v_c implied by standard moment-size scaling relations (14) were greater than 2 km s^{-1}, indicating that the ruptures were fast, whereas the majority of the group A events were slow earth-

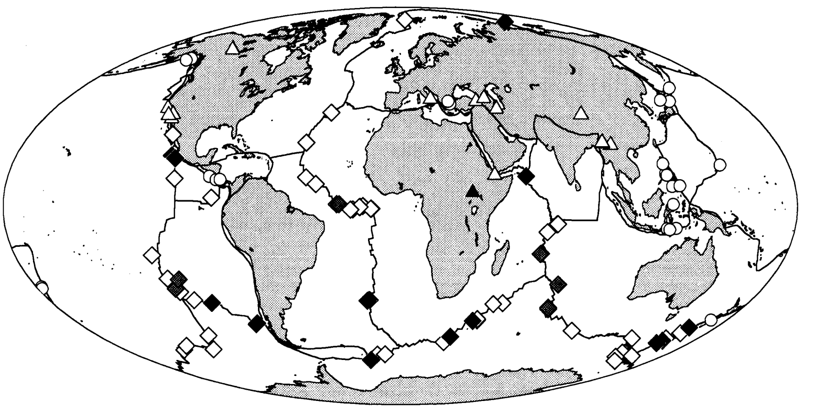

Fig. 1. Map showing continents, plate boundaries, and epicenters of 107 earthquakes analyzed in this study: group A (diamonds), group B (circles), and group C (triangles). Events testing positive for slow precursors are indicated by filled (99% CL) and shaded (95% CL) symbols.

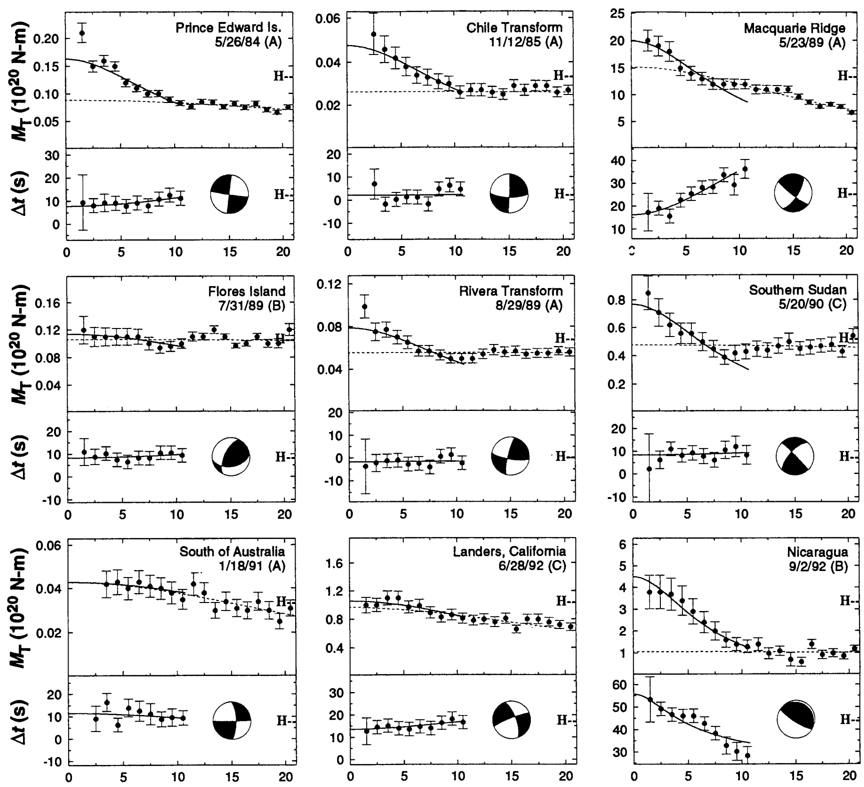

Fig. 2. Source spectra for nine representative earthquakes. Each panel shows amplitude (upper graph) and phase-delay (lower graph) spectra for the earthquake identified by region name, date, and group (in parentheses). Points and 1σ error bars are data; solid lines are least squares fits of Eqs. 1 and 2 at frequencies less than 10 mHz, and dashed lines are fits in the band from 10 to 20 mHz. Phase-delay spectra are referenced to the NEIC origin time (zero of the lower vertical axis). Plots are centered on the Harvard CMT (7) moment and centroid time shift (tick marks labeled H). The beach ball inset shows the orientation of the principal double couple of the Harvard CMT source mechanism. Five of these earthquakes test positively for slow precursors: Prince Edward Island, Chile Transform, Macquarie Ridge, Rivera Transform, and Southern Sudan.

quakes ($v_c < 1$ km s^{-1}) (Fig. 3). Although it has long been appreciated that some transform-fault earthquakes are slow (*15*), systematic surveys of this unexplained phenomenon have been lacking (*16*). The data in Fig. 3 indicate that most intermediate-magnitude ($6 \leq M_W \leq 7$) events on the ocean ridge–transform system are slow earthquakes.

The small, slow earthquakes in group A tend to have large $\tau_c/\Delta t_1$ ratios, indicative of slow precursors (Fig. 4). We let H_0 = {*E* was ordinary} be the null hypothesis that the source time function of an earthquake *E* was zero before its high-frequency origin time ($t = 0$) and nonnegative after this time (*17*). Taylor expansions about $\omega = 0$ relate the four parameters in Eqs. 1 and 2 to the first four polynomial moments of the source time function (*18*). If H_0 is true, then inequalities among the polynomial moments require (*3*) that

$$\Delta t_1 > 0 \qquad (3)$$

$$\Delta t_1 \sqrt{2(1 + \sqrt{1 + 8\alpha})} - \tau_c > 0 \qquad (4)$$

and

$$\alpha + 1/8 > 0 \qquad (5)$$

In addition, H_0 implies that the group delay of the source time function must be positive. If Eq. 2 applies up to an angular frequency ω_{max}, then differentiation gives (*3*)

$$\alpha < 1 + \omega_{max}^{-2}\Delta t_1^{-2} \qquad (6)$$

We tested the null hypothesis H_0 against the alternative H_1 = {*E* had a slow precursor} by evaluating whether the parameters estimated for *E* violated inequalities 3 to 5. We used inequality 6 with $\omega_{max}/2\pi = 10$ mHz as an a priori constraint in determining the left side of inequality 4. We found that H_0 was rejected in favor of H_1 at the 99% confidence level (CL) for 14 of the 107 earthquakes in our sample; at the 95% CL, H_0 failed for an additional six events (Table 1). All earthquakes testing positive for slow precursors failed to satisfy inequality 4; that is, their durations were too long relative to their centroid time shifts to be consistent with no moment release before their high-frequency origin times (*19*). Two events shown in Fig. 2, the Prince Edward Island earthquake of 26 May 1984 and the great Macquarie Ridge earthquake of 23 May 1989, had enough upward curvature in their time-shift spectra that they also failed to satisfy inequality 5 at the 95% CL and 99% CL, respectively. The 29 August 1989 event on the Rivera Transform (Fig. 2) showed a small, negative centroid time shift ($\Delta t_1 = -1.7 \pm 1.3$ s), thus violating inequality 3, although only at the 80% CL.

The set that tested positively for slow precursors at the 95% CL contains 19 earthquakes from group A and 1 from group C (Table 1). For all of the earthquakes in plate-convergence zones (group B), H_0 was acceptable. The lone continental event violating H_0 was the Sudan earthquake of 20 May 1990 (Fig. 2), a slow, complex earthquake with a predominantly left-lateral focal mechanism that initiated a peculiar, 50-day sequence of large events on the Aswa transform fault zone (*20*). All other precursor-positive sources in Table 1 were slow earthquakes on the ocean ridge–transform system. They were more or less uniformly distributed, occurring on slow-spreading as well as fast-spreading plate boundaries (Fig. 1). Three were on the Macquarie and one was on the Sandwich transforms, which are of the ridge-trench type. Strike-slip events predominate, although the set includes a variety of focal mechanisms (*21*).

We checked the results of the hypothesis-testing procedure by inverting broadband (1 to 50 mHz) combinations of free-oscillation, surface-wave, and body-wave spectra for the source time functions of selected events, using the procedures described by Ihmlé *et al.* (*1*). For the well-studied recent earthquakes in California (Landers, for example), our source time functions agreed with the conclusions drawn from the near-field data: these events were fast ruptures with negligible slow precursors (*22*). In the case of the slow, tsunamigenic Nicaragua earthquake of 2 September 1992 (Fig. 2), the source time function recovered by spectral inversion out to 50 mHz (*13*) also had no moment release before the high-frequency origin time, which is consistent with the results of other teleseismic studies (*23*).

Similar inversions done for a subset of the precursor-positive earthquakes [see (*1*), for example] confirmed that the spectral data could not be satisfied by one-sided moment-release histories initiated at the high-frequency origin times. The source time functions that match both the low-frequency data (including the slope breaks in the amplitude spectra at 6 to 12 mHz) and the teleseismic *P* wave forms (showing no evidence of a precursor) can be represented as the sum of two components (*1*, *3*): (i) an emergent, smooth episode of moment release at least 200 s in total duration, punctuated near its peak by (ii) a brief, often complex episode of moment-rate pulses that begins at (or just after) the high-

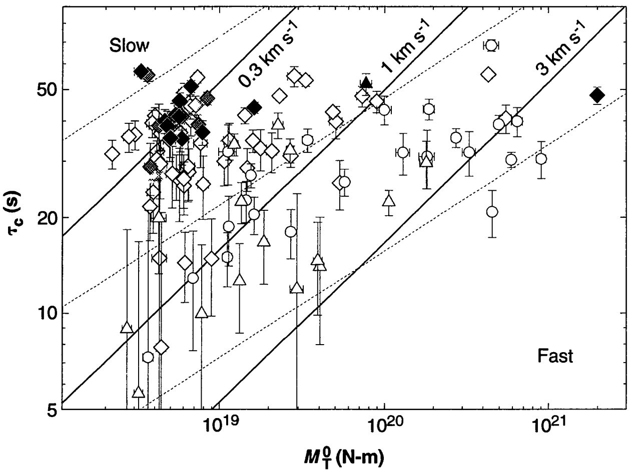

Fig. 3. Characteristic duration τ_c versus total seismic moment M_T^0 (log-log scale). Values and 1σ errors from low-frequency (<10 mHz) spectra are plotted for earthquakes in groups A (diamonds), B (circles), and C (triangles). Events testing positive for slow precursors are indicated by filled (99% CL) and shaded (95% CL) symbols. Solid and dashed lines show characteristic velocities v_c derived from L_c^2 and L_c^3 scaling relations, respectively (*14*). All but one of the precursor-positive events, and most group A events in general, are slow earthquakes with $v_c < 1$ km s^{-1}. The exception is the great Macquarie Ridge earthquake of 23 May 1989.

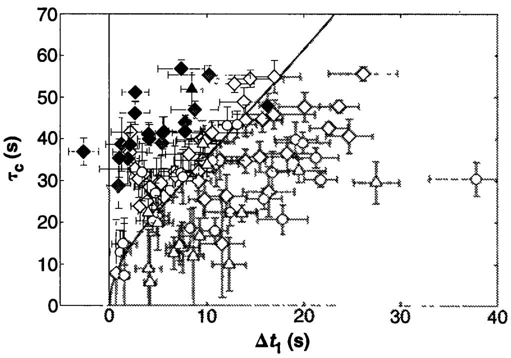

Fig. 4. Characteristic duration τ_c versus centroid time shift Δt_1. Values and 1σ errors estimated from the low-frequency (<10 mHz) spectra are plotted for earthquakes in groups A (diamonds), B (circles), and C (triangles). Events testing positive for slow precursors are indicated by filled (99% CL) and shaded (95% CL) symbols. One precursor-negative event (Nicaragua, 2 September 1992) lies off plot at $\Delta t_1 = 56 \pm 5$ s, $\tau_c = 68 \pm 3$ s. The zero of the horizontal axis is the NEIC origin time. The line separating white and shaded fields is the locus of $\tau_c = \Delta t_1\sqrt{2(1+\sqrt{1+8\alpha})}$ for α equal to the right side of inequality 6.

Table 1. Slow-precursor detections by earthquake groups.

Group	Number	Events for which H_0 was rejected	
		CL (%)	Date, time, and mechanism*
A	68	99	78.08.10.16.53.46 (S) 80.11.01.22.52.24 (S) 83.04.08.02.28.28 (S) 84.05.26.03.59.08 (S) 85.01.31.04.33.04 (C) 85.11.12.03.34.22 (S) 86.12.25.17.17.42 (S) 88.03.21.23.31.24 (N) 89.05.23.10.55.12 (S) 89.08.29.04.16.25 (S) 90.09.17.13.47.35 (S) 91.03.11.21.16.04 (S) 92.06.22.04.00.46 (S)
		95	84.01.16.12.27.18 (C) 84.09.17.06.41.52 (S) 85.05.16.14.20.34 (S) 85.06.06.02.40.21 (S) 86.12.28.20.04.44 (S) 87.07.08.11.50.22 (N)
B	23	95	None
C	16	99	90.05.20.02.22.07 (C)

*Year.month.day.hour.minute.second (mechanism): N (normal), S (strike-slip), or C (complex) (*21*).

frequency origin time. The second component is an ordinary earthquake sequence—a fast, jerky rupture propagating at speeds comparable to the Rayleigh velocity; it dominates the spectrum at frequencies above the slope break and generates the only easily visible signals on seismograms at teleseismic distances, including the *P* waves that fix the high-frequency origin time. The first component is a "quiet earthquake" that radiates teleseismically detectable energy only at low frequencies (*24*).

According to this compound-source model, the low-frequency spectral character of a slow earthquake depends on the relative sizes and timing of these two components. The Macquarie Ridge earthquake (23 May 1989) is an example in which the slow component was only about one-third the moment of the fast component, but its temporal centroid occurred several tens of seconds earlier, giving a phase-delay spectrum with a small centroid time shift and a strong upward curvature (Fig. 2). The slow component of the Nicaragua earthquake (2 September 1992), on the other hand, was at least twice as big as its fast component, and its centroid occurred several tens of seconds later; hence, the centroid time shift of the composite event was large and its phase-delay spectrum curves downward. The three other examples of slow earthquakes in Fig. 2—all precursor-positive events on ridge-ridge transforms—have slow components with sizes and temporal centroids comparable to the fast ruptures; their amplitude spectra have slope breaks near 10 mHz and nearly flat phase-delay spectra.

With the interesting exception of the Sudan earthquake, which occurred in the East Africa Rift system, the slow precursors identified here and in other studies (*1–3*) have thus far been associated with earthquakes confined to oceanic plates (including subducting plates). It is plausible, therefore, that the mechanism of this phenomenon arises from rheological stratification intrinsic to the oceanic lithosphere. Quiet earthquakes, for instance, could be confined to upper-mantle peridotites below the usual seismogenic zone, near the transition from a velocity-weakening to a velocity-strengthening rheology. In the case of the Macquarie Ridge event, the center of low-frequency radiation was deeper by 10 km or more than that at high frequencies (*1*), which lends some support to this conjecture.

Although slow and silent earthquakes have been observed on strainmeters in Japan and other regions (*25*), we know of no near-field detections of short-term slow precursors large enough to satisfy the low-frequency data presented here. We have also been unsuccessful in detecting precursory signals as first-arrival wave forms (*1*). The absence of such signals is not inconsistent with the existence of slow precursors (*1*, *24*), but our identifications should be considered tentative until more direct observations become available. Because most earthquakes with apparent slow precursors occur in oceanic regions far removed from continents and large islands, collecting definitive near-field observations may be especially difficult.

REFERENCES AND NOTES

1. P. F. Ihmlé, P. Harabaglia, T. H. Jordan, *Science* **261**, 177 (1993).
2. H. Kanamori and J. Cipar, *Phys. Earth Planet. Inter.* **9**, 128 (1974); I. L. Cifuentes and P. G. Silver, *J. Geophys. Res.* **94**, 643 (1989).
3. T. H. Jordan, *Geophys. Res. Lett.* **18**, 2019 (1991).
4. ———, P. F. Ihmlé, P. Harabaglia, *Eos* **72**, 201 (1991). The ocean ridge–transform system is defined to be the plate-boundary deformation zones of the mid-ocean spreading centers and associated transform faults, including oceanic ridge–trench transforms such as the Macquarie and Sandwich transform faults.
5. We processed the long-period, vertical-component seismograms for 130 earthquakes with Harvard CMT moments greater than 2×10^{18} N-m (newton-meters) that occurred on the ocean ridge–transform system from 1978 to 1992. We discarded earthquakes that had less than six records with good signal-to-noise ratios in the band from 2 to 5 mHz, eliminating most events with $M_T^0 < 3.5 \times 10^{18}$ N-m ($M_W < 6.3$). Group A comprises the remaining 67 events plus the large Romanche Transform earthquake of 14 March 1994.
6. Earthquakes in groups B and C were chosen to sample the various stress regimes and tectonic subprovinces of subduction zones and continents, respectively, with emphasis on events studied by others to verify our spectral estimation procedures and on strike-slip events to compare with those in group A.
7. A. M. Dziewonski, T.-A. Chou, J. Woodhouse, *J. Geophys. Res.* **86**, 2825 (1981); A. M. Dziewonski and J. H. Woodhouse, *ibid.* **88**, 3247 (1983). Harvard CMT solutions are published on a regular basis in *Physics of the Earth and Planetary Interiors*.
8. The low-frequency, network-averaged data used in this study are well described by a source that has a constant mechanism tensor $\hat{\mathbf{M}}$, is spatially concentrated at the source centroid $\mathbf{r}_1$, and is extended over a time interval that is short compared to that of the wave periods (*26*). The far-field excitation is then specified by a moment-rate function *f*(*t*), whose Fourier transform can be written

$$\int_{-\infty}^{\infty} f(t)e^{-i\omega(t-t_0)}\,dt = M_T(\omega)e^{-i\omega\Delta t(\omega)}$$

where $M_T(\omega)$ is the total moment (amplitude) spectrum, and $\Delta t(\omega)$ is the time-shift (phase-delay) spectrum referenced to t_0, here taken to be the NEIC high-frequency origin time. Both $M_T(\omega)$ and $\Delta t(\omega)$ are even functions of frequency.
9. We used vertical-component seismograms from the IDA, GEOSCOPE, GSN, CDSN, and IRIS networks. We discarded seismograms with nonlinearities, low signal-to-noise ratios, timing errors, or large quasi-Love waves caused by Coriolis coupling (*1*), retaining as few as 6 and as many as 39 in the spectral analysis of each event.
10. M. A. Riedesel, T. H. Jordan, A. F. Sheehan, P. G. Silver, *Geophys. Res. Lett.* **13**, 609 (1986); M. A. Riedesel and T. H. Jordan, *Bull. Seismol. Soc. Am.* **79**, 85 (1989). The complex Fourier spectrum for each observed and synthetic seismogram was integrated over narrow (~0.1-mHz) intervals centered on the average eigenfrequencies of the fundamental modes, and a phase-delay time relative to the synthetic seismogram was calculated from the peak of a cross-correlation function constructed by summing products of the complex-valued spectral integrals over 1-mHz bands; we then obtained $\Delta t(\omega)$ by averaging the phase-delay times over the network.
11. P. G. Silver and T. H. Jordan, *Geophys. J. R. Astron. Soc.* **70**, 755 (1982); (*26*). In the version of the algorithm used here, the squared-amplitude spectrum for each seismogram was integrated over 1-mHz bands, and the integrals for all seismograms were inverted with an estimator optimized to account for the bias and variance due to aspherical heterogeneity, errors in the assumed source mechanism, and ambient seismic noise.
12. We computed synthetic seismograms by complete mode summation from the radially anisotropic Preliminary Reference Earth Model (PREM) of A. M. Dziewonski and D. L. Anderson [*Phys. Earth Planet. Inter.* **25**, 297 (1981)]. We corrected the modes for aspherical heterogeneity using the S12/WM13 model of W.-J. Su, R. L. Woodward, and A. M. Dziewonski [*J. Geophys. Res.* **99**, 6945 (1994)], which represents isotropic, aspherical heterogeneity up to spherical harmonic degree 12, and the asymptotic approximations of J. Woodhouse and A. Dziewonski [*J. Geophys. Res.* **89**, 5953 (1984)]. At frequencies greater than 7 mHz, we corrected the fundamental spheroidal modes using the degree-36 phase-velocity maps of G. Ekström, J. Tromp, and E. W. Larson [*Eos* **74**, 438 (1993)]. From an analysis of the amplitude spectra of well-constrained sources (*1*), we found that the PREM attenuation structure is superior to the more recently published model of R. Widmer, G. Masters, and F. Gilbert [*Geophys. J. Int.* **104**, 541 (1991)]. We investigated the effects of near-source crustal and upper-mantle structure on source-spectrum estimation by computing synthetics for various oceanic and continental models using the adiabatic-mode approximation [A. Levshin, *Ann. Geophys.* **3**, 511 (1985)], and we found them to be small. Aspherical mode coupling not included in the asymptotic approximations, including Coriolis coupling, was also shown to have a negligible effect on source-spectrum estimation (*1*).
13. P. F. Ihmlé, thesis, Massachusetts Institute of Technology (1994).
14. The characteristic velocity is $v_c = L_c/\tau_c$, where L_c is an

appropriate source dimension defined in terms of the second central moment of the Backus stress glut $\Gamma(\mathbf{r},t)$ (*27*). The contours in Fig. 3 correspond to the $M_T^0 \sim L_c^3$ scaling relation of H. Kanamori and J. W. Given [*Phys. Earth Planet. Inter.* **27**, 8 (1981)] and the L_c^2 scaling of C. H. Scholz [*Bull. Seismol. Soc. Am.* **84**, 215 (1994)]. The latter scaling is thought to be more appropriate for the interplate, strike-slip events that dominate our sample.

15. H. Kanamori and G. S. Stewart, *Phys. Earth Planet. Inter.* **11**, 312 (1976); *ibid.* **18**, 167 (1979); E. A. Okal and L. M. Stewart, *Earth Planet. Sci. Lett.* **57**, 75 (1982); A. G. Prozorov and F. J. Sabina, *Geophys. J. R. Astron. Soc.* **76**, 317 (1984).
16. In a survey of anomalous free-oscillation excitations during the 2-year period 1978–1979, Beroza and Jordan (*27*) identified 14 slow earthquakes with $M_W \geq 6.2$; all were in oceanic lithosphere, and 11 were on oceanic transform faults.
17. The source time function is the time derivative of stress glut contracted against an average mechanism tensor $\hat{\mathbf{M}}$ and integrated over the source volume V:

$$f(t)=\frac{1}{\sqrt{2}}\int_V \dot{\Gamma}(\mathbf{r},t):\hat{\mathbf{M}}\,dV(\mathbf{r})$$

We assume that $f(t)$ is a nonnegative function, which permits local slip reversals provided that the net slip at any time has a nonnegative projection onto $\hat{\mathbf{M}}$.

18. For transients beginning at t_0 and ending at t_∞, the source parameters are defined in terms of the moments

$$\mu_p=\int_{t_0}^{t_\infty} f(t)(t-t_0)^p dt,\ p=0,1,2,\ldots$$

and associated central moments $\hat{\mu}_p$ (*3*): $M_T^0=\mu_0$, $\Delta t_1=\mu_1$, $\tau_c=2\hat{\mu}_2^{1/2}$, and $\alpha=\hat{\mu}_3/2\mu_1^3$. The quantities M_T^0 and Δt_1 are the zero-frequency intercepts of $M_T(\omega)$ and $\Delta t(\omega)$, respectively, and τ_c and α are proportional to the downward curvatures of the spectra at $\omega = 0$. Equations 1 and 2 conform to these definitions, but they fix the higher moments ($p \geq 4$) to be special combinations of the low-order source parameters. Errors due to these choices of higher moments will not appreciably bias the estimates of the low-order parameters at frequencies less than $(t_\infty - t_0)^{-1}$. The source spectra were generally observed to vary slowly and smoothly out to 10 mHz, consistent with this criterion.

19. A typical example is the intermediate-magnitude ($M_W = 6.4$) Chile Transform earthquake of 12 November 1985, whose spectra are shown in Fig. 2. The centroid time shift determined from the phase-delay spectrum was $\Delta t_1 = 2.1 \pm 1.2$ s, essentially identical to the Harvard CMT value of 2.8 s. From 10 to 20 mHz, the amplitude spectrum was flat and extrapolated to a seismic moment of $(2.6 \pm 0.3) \times 10^{18}$ N-m, slightly smaller than the Harvard CMT value of 3.4×10^{18} N-m. The amplitude spectrum rose systematically below 10 mHz, however, indicating that this earthquake was a slow event; fitting Eq. 1 to these low-frequency values gave $M_T^0 = (4.8 \pm 0.4) \times 10^{18}$ N-m and $\tau_c = 39 \pm 4$ s. The integral of the likelihood function over the region of parameter space defined by inequalities 4 and 6 was less than 1%, so we rejected H_0 in favor of H_1 at the 99% CL.
20. R. Gaulon, J. Chorowicz, G. Vidal, B. Romanowicz, G. Roult, *Tectonophysics* **209**, 87 (1992). On the basis of the May–July 1990 earthquake sequence and supplementary field evidence, these investigators argued that the northwest-southeast–trending Aswa lineament is an active, left-lateral, intracontinental transform fault connecting the eastern and western branches of the East African Rift. They derived a Rayleigh-wave moment of 8.2×10^{19} N-m for the 20 May 1990 main shock, 50% larger than the Harvard CMT value and nearly twice the moment they computed from higher frequency body waves. These observations are consistent with the rapid roll-off in our amplitude spectrum at low frequencies (Fig. 2), which gave $M_T^0 = (7.7 \pm 0.6) \times 10^{19}$ N-m and $\tau_c = 52 \pm 4$ s. The Sudan earthquake thus plots in the slow-earthquake field of Fig. 3, and under H_0, its long duration is inconsistent at the 99% CL with its small centroid time shift, $\Delta t_1 = 8.4 \pm 1.2$ s (Fig. 4). The latter is in good agreement with the Harvard CMT value of 7.8 s.
21. The two normal-fault events (labeled N in Table 1) occurred on 8 July 1988, near Easter Island, and on 21 March 1988, in the Laptev Sea near the intersection of the Arctic mid-ocean ridge with the Asian continental slope. Three entries were designated as complex (labeled C), because they had moment tensors with significant compensated-linear-vector-dipole components; in most cases involving large moment release, such mechanisms are thought to be indicative of shear failures on multiple fault planes [C. Frohlich, *Science* **264**, 804 (1994)].
22. California earthquakes in our sample are Superstition Hills (24 November 1987) [D. C. Agnew and F. K. Wyatt, *Bull. Seismol. Soc. Am.* **79**, 480 (1989)], Loma Prieta (18 October 1989) [M. J. S. Johnston, A. T. Linde, M. T. Gladwin, *Geophys. Res. Lett.* **17**, 1777 (1990)], and Landers (28 June 1992) [M. J. S. Johnston, A. T. Linde, D. C. Agnew, *Bull. Seismol. Soc. Am.* **84**, 799 (1994)]. In the case of Landers, for example, the slight upward curvature of the phase-delay spectrum seen in Fig. 2 is consistent with the negative skewness of the source time function obtained by H. Kanamori, H.-K. Thio, D. Dreger, and E. Hauksson [*Geophys. Res. Lett.* **19**, 2267 (1992)] from waveforms recorded near the epicenter.
23. H. Kanamori and M. Kikuchi, *Nature* **361**, 714 (1993); S. F. Ide, F. Imamura, Y. Yoshida, K. Abe, *Geophys. Res. Lett.* **20**, 863 (1993).
24. "Quiet earthquake" is an infraseismic event that excites low-frequency (<5 mHz) free oscillations but does not produce detectable wave groups at teleseismic distances (*1*, *3*). This type of infraseismic source was postulated by Beroza and Jordan (*27*) to explain anomalous episodes of low-frequency mode excitation detected by the International Deployment of Accelerometers network during periods when no ordinary earthquake was observed. Experiments with synthetic seismograms for high-gain, broadband stations indicate that quiet earthquakes have characteristic durations greater than 200 s and amplitude spectra that roll off more rapidly than ω^{-3}.
25. I. S. Sacks, S. Suyehiro, A. T. Linde, J. A. Snoke, *Nature* **275**, 599 (1978); A. T. Linde, S. Suyehiro, S. Miura, I. S. Sacks, A. Takagi, *ibid.* **334**, 513 (1988); H. Kanamori, *Geophys. Res. Lett.* **16**, 1411 (1989).
26. P. G. Silver and T. H. Jordan, *J. Geophys. Res.* **88**, 3273 (1983).
27. G. C. Beroza and T. H. Jordan, *ibid.* **95**, 2485 (1990).
28. We thank P. Harabaglia and R. Cicerone for assistance and G. Ekström, J. Tromp, and E. Larson for the use of their unpublished phase-velocity maps. This research was sponsored by the National Science Foundation under grant EAR-9305081 and the National Aeronautics and Space Administration under grant NAG5-1905. P.F.I. was supported in part by grants from the Huber-Kudlich Stiftung and Sunburst Fonds.

29 July 1994; accepted 29 September 1994

Nanoscale Imaging of Molecular Adsorption

Heng Cai, Andrew C. Hillier,* Kevin R. Franklin, C. Craig Nunn, Michael D. Ward*

In situ atomic force microscope observations were made of the adsorption of anions (1− or 2−) of the organic diacid 5-benzoyl-4-hydroxy-2-methoxybenzenesulfonic acid from aqueous solution onto the (0001) surface of hydrotalcite (HT), a layered clay. This adsorption process is believed to mimic the ion-exchange reactions that occur within the layers of HT and other layered clays. Atomic force microscope images of the (0001) surfaces of HT, acquired in aqueous solutions, reveal an ordered structure with respect to magnesium and aluminum atoms. In the presence of the anions, atomic force microscopy indicates pH-dependent adsorption onto the formally cationic HT surface. The anion coverage is governed by electroneutrality and steric interactions between the bulky anions within the adsorbed layer, whereas the orientation of the anions with respect to the HT surface is dictated by coulombic interactions and hydrogen bonding between the anion's sulfonate moiety and clay hydroxyl triads. These observations reveal that the reversible adsorption of molecular species can be examined directly by in situ atomic force microscopy, providing details of surface stoichiometry and adlayer symmetry on the local, molecular level.

Layered clays are of scientific and technological interest because of their use as ion-exchange materials (*1*), catalysts (*2*), antacids (*3*), catalytic supports (*4*), and modified electrodes (*5*). The observation that cationic clays preferentially adsorb one enantiomer when exposed to mixtures of L- and D-histidine has led to the suggestion that the stereoselective adsorption-desorption of molecules on clays may be related to the origin of chirality in living systems (*6*). Although conventional analytical methods have provided considerable insight into the reactivity and structure of layered clays, local characterization at the molecular level is lacking. In this report, we describe the use of atomic force microscopy (AFM) to visualize, in situ, the formation and structure of highly ordered adlayers of individual organic anions on the cationic surface of a layered clay, hydrotalcite (HT). These studies reveal the local structure and symmetry of adsorbed molecules, which may mimic the arrangement of these species when intercalated in HT.

Hydrotalcite, $Mg_6Al_2(OH)_{16}CO_3 \cdot 4H_2O$,

H. Cai and C. C. Nunn, Unilever Research U.S.–Edgewater Laboratory, 45 River Road, Edgewater, NJ 07020, USA.
A. C. Hillier and M. D. Ward, Department of Chemical Engineering and Materials Science, University of Minnesota, Amundson Hall, Minneapolis, MN 55455, USA.
K. R. Franklin, Unilever Research–Port Sunlight Laboratory, Quarry Road East, Bebington, Wirral L63 3JW, UK.

*To whom correspondence should be addressed.